# Journal of Materials Chemistry A

Accepted Manuscript


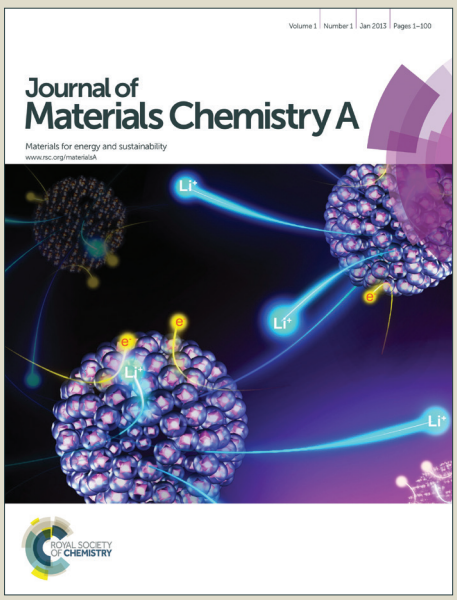





ROYAL SOCIETY OF CHEMISTRY

www.rsc.org/materialsA

Journal Name

RSCPublishing

ARTICLE

# Honeycomb-like $NiMoO_4$ Ultrathin Nanosheet Arrays for High-performance Electrochemical Energy Storage†

Kang Xiao,[a] Lu Xia,[a] Guoxue Liu,[a] Suqing Wang,[a] Liang-Xin Ding*[a] and Haihui Wang*[ab]

Cite this: DOI: 10.1039/x0xx00000x

Received 00th January 2012,
Accepted 00th January 2012

DOI: 10.1039/x0xx00000x

www.rsc.org/

Supercapacitors and Li-ion batteries are two types of electrical energy storage devices. To satisfy the increasing demand for high-performance energy storage devices, traditional electrode materials, such as transition metal oxides, conducting polymers and carbon-based materials, have been widely explored. However, the results obtained to date remain unsatisfactory, and the development of inexpensive electrode materials (especially for commercial manufacturing) with superior electrochemical performance for use in supercapacitors and in Li-ion batteries is still needed. The as-prepared $NiMoO_4$ nanosheets (NSs) with interconnecting nanoscale pore channels and an ultrathin structure provide a large electrochemical active area, which facilitates electrolyte immersion and ion transport and provides effective pathways for electron transport. Therefore, the as-prepared $NiMoO_4$ NS electrode exhibits a high specific capacity and an excellent rate capability and cycling stability in supercapacitors and in Li-ion batteries. Moreover, a high energy density (43.5 W h $kg^{-1}$ at 500 W $kg^{-1}$) was obtained for the symmetric supercapacitor (SSC) composed of two sections of $NiMoO_4$ NSs.

## 1. Introduction

Because of the increasing concerns regarding the energy crisis and environmental pollution, considerable efforts have been focused on the design and development of advanced energy storage devices.[1-3] Among the various electrochemical energy storage and conversion devices, supercapacitors (SCs) and Li-ion batteries (LIBs) are two of the most popular types in consumer electronic devices and electric vehicles.[4,5] Carbon materials, such as graphene and carbon nanotubes, have been widely used directly for the current LIB anodes, commercial SCs and sodium ion batteries due to their advantages of low cost, superior rate performance and cycle life.[6-12] However, the relatively low charge storage capability of carbon-based materials (theoretically, 372 mA h $g^{-1}$ in LIB anodes[13] and <150 F $g^{-1}$ in SCs[14]) has seriously limited their practical applications in energy storage. Meanwhile, transition metal oxides, such as NiO,[15,16] CoO,[17] $Co_3O_4$,[18,19], $Fe_2O_3$[20,21], and $V_2O_5$[22]are generally considered to be promising electrode materials for the next generation of energy storage devices because they possess a higher charge storage capability compared with carbon materials. Unfortunately, most of these metal oxides often suffer from low capacitance and unsatisfactory cycling stability and/or rate performance due to their intrinsic properties, including low electrical conductivity and poor mechanical stability, which hinders the electrochemical reactions.[23]

Recently, binary metal oxides, such as $NiCo_2O_4$, $MnCo_2O_4$, $NiMoO_4$, $CoMoO_4$, and $MnMoO_4$, have attracted significant attention for their potential for energy storage because they possess multiple oxidation states and significantly better electrical conductivity compared with single-component oxides, resulting in higher capacitances.[24-26] Among these binary metal oxides, $NiMoO_4$ has attracted significant research interest because of its excellent electrical conductivity and remarkable electrochemical energy storage performance resulting from the high electrical conductivity of the Mo element and the high electrochemical activity of the nickel ion.[27,28] However, developing methods to improve the electrochemical performance of binary metal oxides and to fully realize the advantages of the active materials for practical applications remains a major challenge. For example, Das and co-workers[29] have synthesized $NiMoO_4{\cdot}nH_2O$ nanorods using a hydrothermal procedure, and the specific capacitances of the $NiMoO_4{\cdot}nH_2O$ nanorods were only 142 F $g^{-1}$ at scan rates of 5 mV $s^{-1}$. Liu and co-workers[30] have reported that $NiMoO_4{\cdot}xH_2O$ nanobundles show a high specific capacitance of 1,136 F $g^{-1}$ at a current density of 2.5 mA $cm^{-2}$, but only 36.1% of this value remained at a high current density of 100 mA $cm^{-2}$.

Nanostructure engineering has been an effective strategy to enhance the electrochemical energy storage properties of LIBs and SCs because the nanostructures could shorten the ion transport pathways and increase the active surface areas, among other effects. Several different types of $NiMoO_4$ nanostructures have been recently synthesized, including nanorods, nanosheets, and nanowires, and their electrochemical performances have been investigated. For example, Wang *et al*[31] have reported the synthesis of $NiMoO_4$ nanorods and hierarchical nanospheres through a hydrothermal method, achieving a high specific capacitance (974.4 and 944.8 F $g^{-1}$

at the current density of 1 A $g^{-1}$). Similarly, Low *et al*[32] have recently proven that the $NiMoO_4$ nanosheet electrode can provide a higher specific capacitance (1,221.2 *vs* 1,091.1 F $g^{-1}$) than $NiMoO_4$ nanorods at a current density of 1 A $g^{-1}$. Furthermore, an asymmetric supercapacitor based on $NiMoO_4$ nanosheets and active carbon as the positive and negative electrodes, respectively, exhibits a high energy density of 60.9 W h $kg^{-1}$. However, the mentioned hydrothermal methods used to prepare the $NiMoO_4$ nanostructures require tedious processing and/or relatively toxic additives, both of which restrict large-scale production and potential applications. Therefore, development of a facile, efficient and economical method is required to prepare nanostructured $NiMoO_4$ with unique morphologies and enhanced energy storage capacity. To the best of our knowledge, the synthesis of $NiMoO_4$ nanostructures through an electrodeposition process is reported here for the first time. In addition, most of the reported lithium storage capabilities of $NiMoO_4$ have focused on its use as a cathode material.[27,28] Therefore, its lithium storage capabilities as an anode material remain unexplored.

Based on these considerations, we report the successful development of a simple electrochemical method coupled with a calcination treatment process to deposit honeycomb-like $NiMoO_4$ ultrathin NSs with porous nanostructures on a conductive Ni foam substrate that was directly used as the electrode for SCs and LIBs. Remarkably, the as-prepared ultrathin mesoporous $NiMoO_4$ NSs exhibited high capacitance/capacity, excellent rate performance, and good cycling stability, presenting a promising difunctional electrode material for high-performance energy storage.

## 2. Experimental Section

### 2.1 Preparation of ultrathin mesoporous $NiMoO_4$ NSs

All of the solvents and chemicals were of reagent quality and were used without further purification. The Ni foam was cleaned with deionized (DI) water, ethanol, and acetone under ultrasonication. Electrodeposition was conducted using a CHI 760E model Electrochemical Workstation (Shanghai) with a standard two-electrode glass cell at room temperature, a platinum plate (1.0 cm × 1.0 cm) as the counter electrode and a piece of clean Ni foam as the working electrode. The Ni Mo precursor NSs were electrodeposited in a solution containing 5 mM $Ni(NO_3)_2$ and 5 mM $Na_2MoO_4$ at -0.5 mA $cm^{-2}$ for 5 min at room temperature. The as-prepared Ni Mo precursor was further calcined at 400 ℃ for 4 h in Ar with a temperature ramp rate of 2 ℃ $min^{-1}$. The mass of $NiMoO_4$ NSs was carefully weighted before electrodeposition and after annealing using electronic scales (averaging 0.4 mg).

### 2.2 Material characterization

The surface morphology and structure of the as-prepared samples were analyzed by field emission scanning electron microscopy (FE-SEM, Quanta 400) and transmission electron microscopy (TEM, FEI, Tecnai™ G2F30). The crystallographic structure of the samples was analyzed using powder X-ray diffraction (XRD, Bruker, D8 ADVANCE) with Ka radiation (λ = 1.5418 Å). The chemical state and composition of the products were analyzed by X-ray photoelectron spectroscopy (XPS, ESCALab250).

### 2.3 Supercapacitor Performance Measurements

The single electrode tests were conducted using an electrochemical workstation (CHI760E) in a three electrode cell, with an SCE reference electrode and a Pt plate counter electrode in 1 M aqueous KOH electrolyte at room temperature. The $NiMoO_4$ NSs were directly used as the working electrode. The SSCs were assembled from two sections of $NiMoO_4$ NS electrode (with the same mass) with a separator, and the electrolyte was 1 M KOH.

### 2.4 Battery Performance Measurements

The cells (CR2025) were assembled in an argon-filled glove box consisting of a piece of $NiMoO_4$-Ni foam and lithium foil separated by a glass fiber membrane and were used for the LIB tests. $LiPF_6$ (1 M) in a solvent mixture of diethyl carbonate (DMC) and ethylene carbonate (EC) (1:1 by mass) was used as the electrolyte. The discharge and charge measurements of the cells were obtained on a Battery Testing System with the voltage ranging from 0.01 to 3.0 V (*vs* $Li/Li^+$) at various current densities. The cyclic voltammetry (CV) studies were also performed on an electrochemical workstation (CHI760E) at a scan rate of 0.5 mV $s^{-1}$.

## 3. Results and Discussion

### 3.1 Morphology and Structural Analysis

The fabrication processes of the $NiMoO_4$ ultrathin mesoporous NSs deposited on Ni foam are schematically illustrated in Figure 1. First, at the surface of the cathode, $NO_3^-$ can be reduced to $OH^-$, as shown in Equation 1. Next, the Ni-Mo hydroxide precursor was co-electrodeposited on the Ni foam, as shown in Equation 2.

$$NO_3^- + 7\ H_2O + 8\ e^- \rightarrow NH_4^+ + 10\ OH^- \quad (1)$$

$$Ni^{2+} + Mo^{6+} + 8\ OH^- \rightarrow NiMo(OH)_8 \quad (2)$$

An annealing treatment at 400℃ in $Ar_2$ along with the thermally induced dehydration of the Ni-Mo hydroxide precursor yielded ultrathin mesoporous $NiMoO_4$ NSs, as described by the following equation:

$$NiMo(OH)_8 \rightarrow NiMoO_4 + 4\ H_2O \quad (3)$$

The crystallographic structures of the as-prepared samples are characterized by X-ray diffraction (XRD) measurements, and the corresponding results are shown in Figure S1 (Supporting Information). It can be observed that there is no diffraction peak pertaining to $NiMoO_4$, except for the peaks from the Ni foam substrate, indicating that the grown $NiMoO_4$ is amorphous[33],

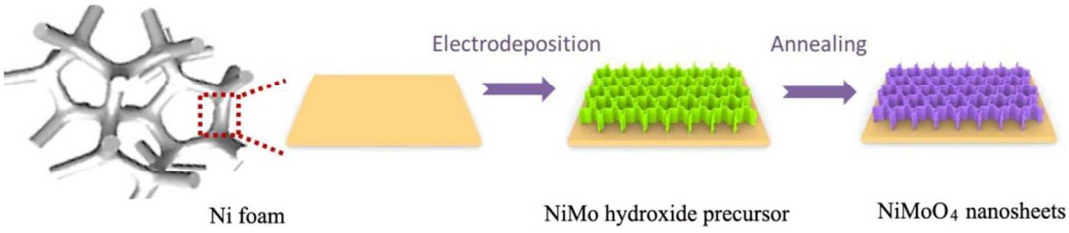


**Figure 1.** Schematic illustration of the fabrication process of the $NiMoO_4$ NSs.

Journal Name

RSCPublishing

ARTICLE

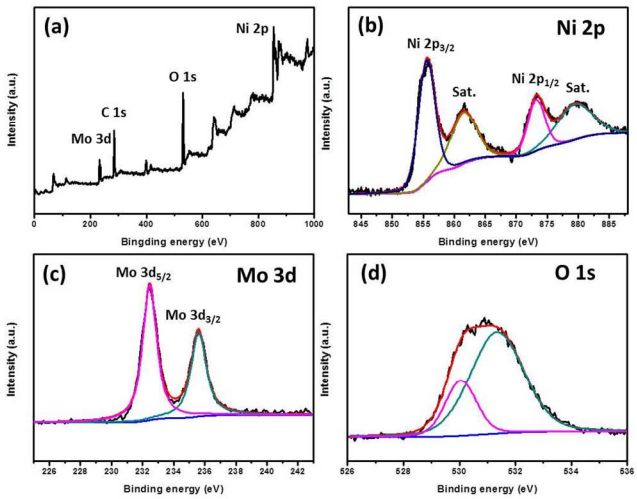


**Figure 2**. XPS spectra of the $NiMoO_4$ NSs. (a) Survey scan, (b) Ni 2p spectrum, (c) Mo 3d spectrum, and (d) O 1s spectrum.

which is further confirmed by the TEM results. The elemental composition and valence state information of the as-synthesized samples are further characterized by X-ray photoelectron spectroscopy (XPS), as presented in Figure 2. The survey spectrum (Figure 2a) primarily shows the presence of Ni, Mo, and O, along with a small quantity of C from the reference. Using a Gaussian fitting method, the Ni 2p emission spectrum was fitted with two spin-orbit doublets and its shakeup satellites (Figure 2b). Two major peaks with binding energies at 873.4 and 855.9 eV correspond to the Ni $2p_{3/2}$ and Ni $2p_{1/2}$ levels, respectively. The spin-energy separation of 17.6 eV is characteristic of $Ni^{2+}$.[34,35] In the Mo 3d high-resolution spectra (Figure 2c), two peaks with binding energies at 232.4 and 235.5 eV correspond to Mo $3d_{5/2}$ and Mo $3d_{3/2}$, respectively, which is characteristic of $Mo^{6+}$.[29] The O 1s XPS spectrum can be divided into two main peaks (Figure 2d). The peak at 530 eV is typical of the metal-oxygen bonds, and the peak at 531.3 eV can be attributed to oxygen ions in low coordination at the surface.[36] The XPS results suggest that the chemical composition of the as-prepared $NiMoO_4$ sample contains $Ni^{2+}$ and $Mo^{6+}$, which is in good agreement with previously reported data.

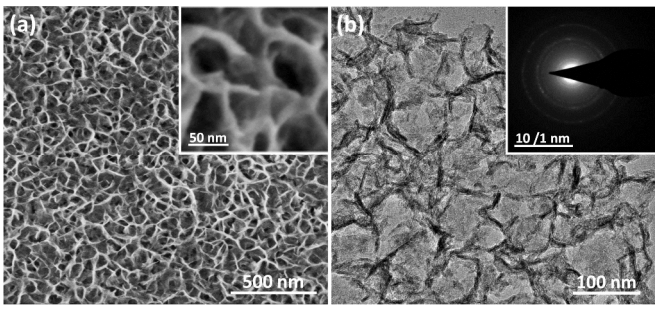


**Figure 3.** (a) SEM images of the $NiMoO_4$ NSs, (b) TEM images of the $NiMoO_4$ NSs.

Figure S2a (Supporting Information) shows the low-magnification SEM image of the Ni-Mo hydroxide precursor. Clearly, the Ni-Mo hydroxide precursor with the microporous structure can be found uniformly developing on the surface of the Ni substrate. The high-magnification SEM image (Figure S2b) of the enlargement region from Figure S2a further reveals the microstructure of the precursor. Evidently, the Ni-Mo hydroxide precursor shows a nanosheet and mesoporous open space microstructure with a honeycomb-like morphology. After the annealing conversion into $NiMoO_4$, the basic morphology of the sample is well-retained without obvious changes induced by annealing (Figure 3a). The as-formed honeycomb-like ultrathin nanosheet structure with abundant open spaces can provide more electroactive surface sites, resulting in effective penetration of the electrolyte and enhanced mass/charge transfer at the electrode/electrolyte interface.[37] The morphology and structure of the as-prepared samples were further investigated by transmission electron microscopy (TEM). Figure 3b shows a panoramic view of the as-synthesized $NiMoO_4$ NSs. The interconnected honeycomb-like characteristic with a distinct dark/light contrast strongly suggested the existence of nanosheets and open space structures, which are in good agreement with the SEM observation. There is no crystalline lattice fringe, as can be observed from the high-resolution TEM (Figure S2c**,** Supporting Information), indicating that the honeycomb-like NSs are amorphous. The selected area electron diffraction (SAED) pattern further proves the amorphous morphology of the $NiMoO_4$ NSs because of a highly ambiguous halo ring (the inset of Figure 3b). The EDX pattern clearly reveals that the product contains the elements Ni, Mo, and O, which agrees with the XPS results (Figure S3, Supporting Information).

### 3.2 Performance of the Supercapacitors

A conventional three-electrode cell with 1 M KOH as the electrolyte, an SCE reference electrode, and a Pt wire as the counter-electrode was used to evaluate the electrochemical performance of the $NiMoO_4$ NSs. Figure 4a presents the CV curves of the $NiMoO_4$ NS electrode at various scan rates ranging from 1 mV $s^{-1}$ to 100 mV $s^{-1}$. A pair of well-defined redox peaks can be observed in all of the CV curves, corresponding to the Faradaic redox reactions, Ni (II) ↔ Ni (III) + $e^-$, which is characteristic of a pseudocapacitive behavior. Furthermore, these CV curves exhibit unchangeable shapes, except for the slight shift in the redox peak position with the increasing scan rates, implying that the ultrathin nanosheet structure is conducive to rapid redox reactions, resulting in superior capacitive and high-rate performance. It is crucial to demonstrate the potential capacitance contribution from the Ni foam substrate. We tested the CV curves of the Ni foam using the same scan rates (Figure S5**,** Supporting Information). The anodic and cathodic currents of the Ni foam are significantly smaller than the $NiMoO_4$ NS-NF composite electrode. Thus, the capacitance of the Ni foam can be neglected. Figure 4b shows that there is a linear relationship between the square root of the scan rate and the current of the redox peaks, indicating that the electrochemical process is a diffusion-controlled process [$OH^-$]. To evaluate the electrochemical capacitive performance of the $NiMoO_4$ NS electrode, galvanostatic charge-discharge (GCD) tests were performed within the potential

Journal Name

RSCPublishing

ARTICLE

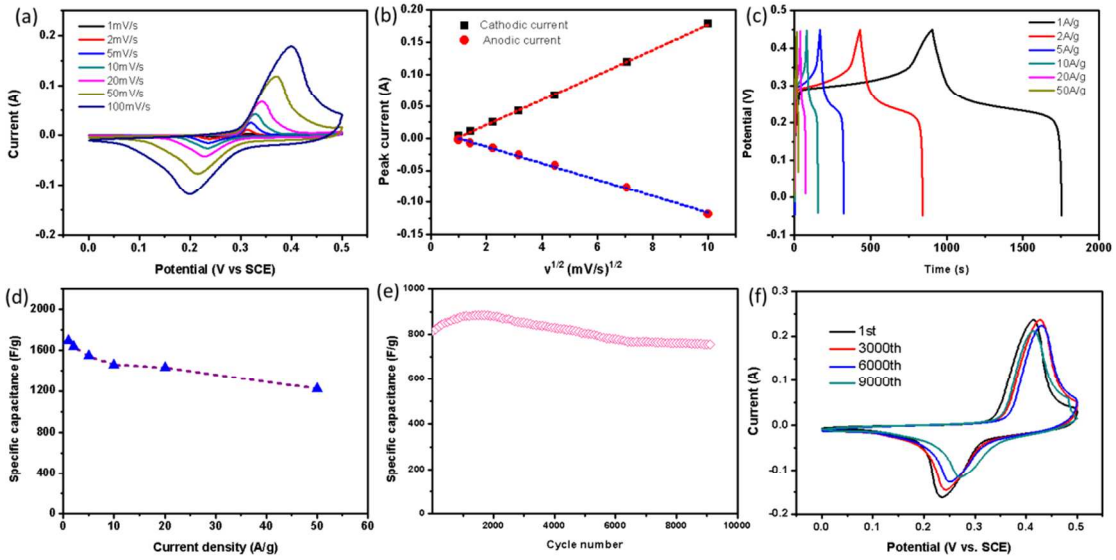


**Figure 4.** (a) CV curves of the $NiMoO_4$ NSs at scan rates ranging from 1 to 100 mV $s^{-1}$. (b) Correlation between *Ip* and $v^{1/2}$ of the $NiMoO_4$ NS electrode. (c) GCD curves of the $NiMoO_4$ NS electrode collected at different current densities. (d) Specific capacitance of the $NiMoO_4$ NS electrode as a function of current density. (e) Cycle performance of the $NiMoO_4$ NS electrode measured at a scan rate of 200 mV $s^{-1}$ for 9,000 cycles. (f) Representative CV curves collected initially and at the 1, 3,000, 6,000 and 9,000 cycles.

window of -0.05 to 0.45 V (vs SCE) at current densities ranging from 1 to 50 A $g^{-1}$. As shown in Figure 4c, the nonlinear shape of the GCD curves further verified the pseudocapacitance behavior. Additionally, the GCD curves of the $NiMoO_4$ NSs show the symmetric nature without an obvious IR drop, indicating again that the amorphous honeycomb-like $NiMoO_4$ NSs exhibit a rapid *I-V* response characteristic and an excellent reversible redox reaction. Figure 4d presents the calculated specific capacitance of the $NiMoO_4$ NS electrode as a function of current density (for the detailed calculation, see Supporting Information). The maximum specific capacitance (1,694 F $g^{-1}$) of the $NiMoO_4$ NSs was achieved at the current density of 1 A $g^{-1}$, which is similar to the values of specific capacitance obtained by CV technique (Figure S4, Supporting Information). Significantly, the specific capacitance remained as high as 1,220 F $g^{-1}$ (72% retention), and even the current density increased to 50 A $g^{-1}$, indicating the outstanding electron transport and ion diffusion ability. To the best of our knowledge, this present capacitance and excellent rate capability are considerably higher compared with most of the previously reported $NiMoO_4$-based pseudocapacitive materials (Table S1, Supporting Information).

The long-term cycling performance is an essential requirement for the practical application of SCs. Figure 4e presents the cycling stability of the $NiMoO_4$ NS electrode at a scan rate of 200 mV $s^{-1}$. As shown in this figure, the capacitance gradually increases during the first 1,200 cycles, which can be attributed to the full activation of the electrode.[38,39] Importantly, the capacitance retains approximately 92.7% of its initial value after 9,000 cycles. The specific CV curves present a slight electrochemical change, revealing the outstanding performance of the cycles (Figure 4f). This retention rate is comparable to the recently reported $NiMoO_4$ electrode (89.2% after 10,000 cycles) described by the Lou group[26] and is significantly higher than most of the previously reported values (Table S1, Supporting Information). The excellent cycling stability can be attributed to the strong contact between the $NiMoO_4$ NSs and the Ni foam and its good structural stability. Figure S6 (Supporting Information) shows the SEM image of the $NiMoO_4$ NS electrode after 9,000 cycles and reveals that there is no obvious structural modification.

To demonstrate the practical application of the amorphous honeycomb-like $NiMoO_4$ NS electrode as high-performance SCs, a simple symmetric supercapacitor (SSC) device was assembled using two sections of the as-grown $NiMoO_4$ NSs electrodes. Figure 5a shows the CV curves of the as-fabricated $NiMoO_4$// $NiMoO_4$-SSC device collected at a scan rate of 50 mV $s^{-1}$ at different working voltages. The data proved that the voltage window of the as-fabricated $NiMoO_4$// $NiMoO_4$-SSCs device can be extended to 1.2 V, and the best operating potential range is from 0-1.0 V. Figure 5b displays the CV curves of the fabricated SSC device at different scan rates ranging from 0-1.0 V. All of the CV curves exhibited a quasi-rectangular shape and did not display a significant change at a high scan rate, indicating that the fabricated SSC device possesses a rapid current response and good capacitive behavior.[40] Figure 5c displays the GCD curves and the relatively symmetric shapes at high current densities, demonstrating the good charge storage performance. The slightly nonlinear shape during the charging process of 1 A $g^{-1}$ was primarily attributed to the redox reaction of metal oxides, which agrees with the CV results.[32] Based on the discharge times, the specific capacitances of the device are calculated as shown in Figure 5d. The $NiMoO_4$//$NiMoO_4$-SSC device achieved the highest specific capacitance (based on the total mass of the active materials of the

Journal Name RSCPublishing

ARTICLE

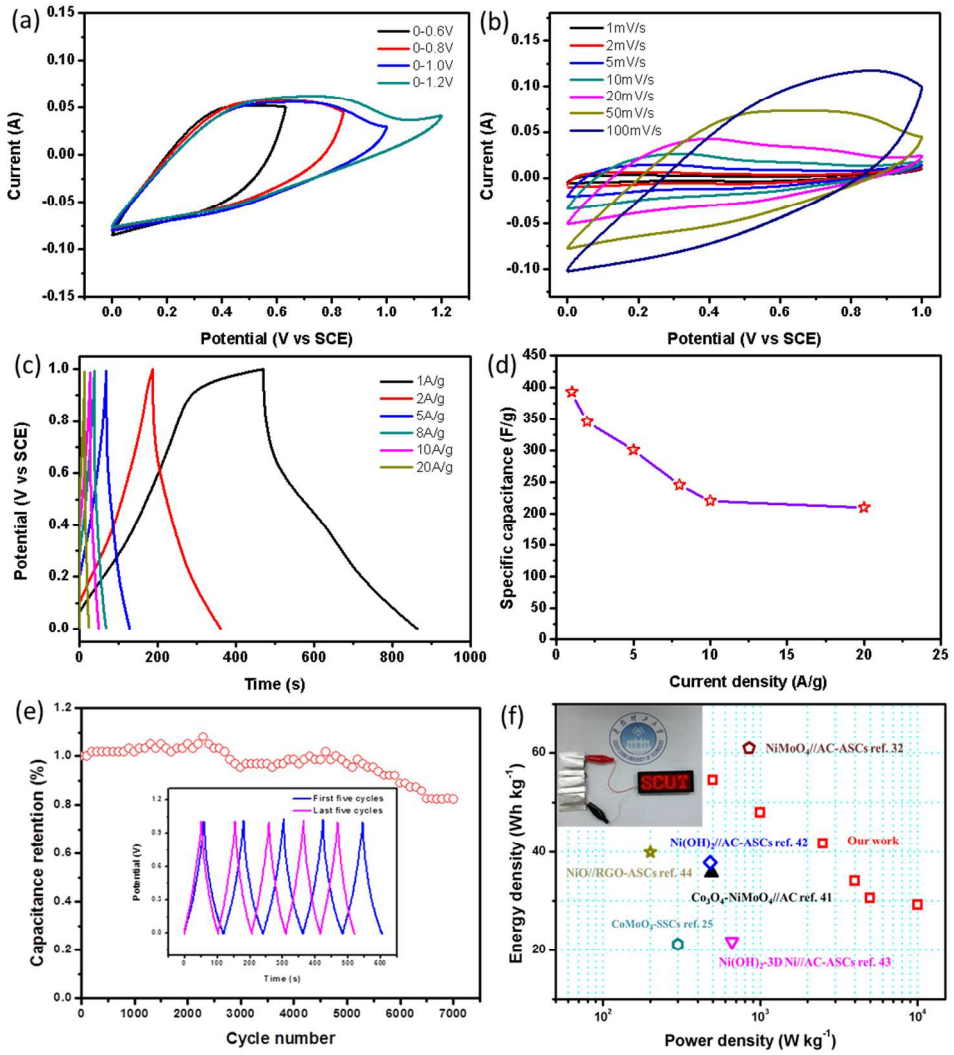


**Figure 5.** (a) CV curves of the $NiMoO_4$ NS//$NiMoO_4$ NS-SSC device collected at different scan voltage windows at 50 mV $s^{-1}$. (b) CV curves of the SSC device at various scan rates over the voltage range of 0-1.0 V. (c) GCD curves of the SSC device at various current densities over the voltage range of 0-1.0 V. (d) The specific capacitance of the SSC device at various current densities. (e) Cycling performance of the SSC device (7,000 cycles). The inset shows the charge-discharge curves. (f) Ragone plot of the SSC device and comparison with other SC devices.

two electrodes) of 392.9 F $g^{-1}$ at 1 A $g^{-1}$ and the capacitance retention of 53.7% at a current density of 20 A $g^{-1}$, demonstrating its good rate capability. The electrochemical stability of the SSC devices was evaluated by a GCD test at a current density of 6 A $g^{-1}$. As shown in Figure 5e**,** the as-fabricated SSC device shows a negligible loss of capacitance after 5,000 cycles (5% capacitance loss) and retained 83% after 7,000 cycles, which can also be observed in the GCD curves of the first and last ten cycles (the inset of Figure 5e).

The energy and power densities are two important parameters for an SC device. Figure 5f compares the energy densities and power densities of the $NiMoO_4$ SSC devices with those recently reported for other SSCs and ASCs (for the detailed calculation, see Supplementary Information). Although there is only a small voltage window for the $NiMoO_4$ SSCs devices, the maximum energy density (54.5 Wh $kg^{-1}$) is slightly lower than the $NiMoO_4$//AC ASCs (60.9 Wh $kg^{-1}$)[32] and higher than those recently reported for other SCs, such as $CoMoO_4$ SSCs (37.25 Wh $kg^{-1}$),[25] $Co_3O_4$-$NiMoO_4$// AC ASCs (37.8 Wh $kg^{-1}$),[41] $Ni(OH)_2$//AC ASCs (35.7 Wh $kg^{-1}$),[42] $Ni(OH)_2$-3D Ni//AC ASCs (24.2 Wh $kg^{-1}$),[43] and NiO//RGO ASCs (39.9 Wh $kg^{-1}$).[44] Additionally, a red light-emitting diodes array (2.7 ~ 3.5 V) can be powered by our SSC devices (three were connected in series, inset in Figure 5f) for 1 min after charging at 10 A $g^{-1}$ for 30 s.

Journal Name RSCPublishing

ARTICLE

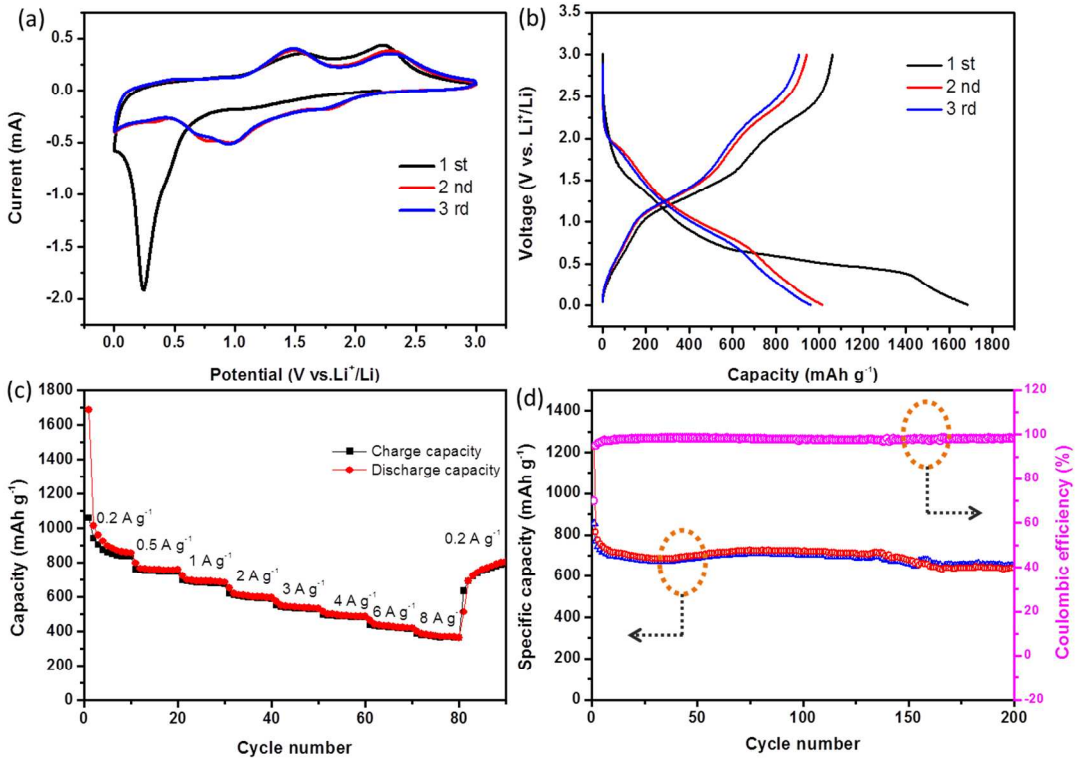


**Figure 6.** (a) CV curves of the $NiMoO_4$ NSs at a scan rate of 0.5 mV $s^{-1}$. (b) Charge-discharge voltage profiles of $NiMoO_4$ NSs for the first three cycles at a current density of 0.2 A $g^{-1}$. (c) The specific capacity of the $NiMoO_4$ NSs at various current densities. (d) Specific capacity and Coulombic efficiency for 200 cycles at 1 A $g^{-1}$ for $NiMoO_4$ NSs.

### 3.3 Performance of the Lithium-Ion Batteries

As another demonstration, the $NiMoO_4$ NSs were also tested as a binder-free anode for LIBs. To understand the Li-ion insertion and extraction process, the CV curves of the $NiMoO_4$ NS electrode were obtained over the potential range of 0.01-3.0 V (*vs* $Li/Li^+$) at a scan rate of 5 mV $s^{-1}$. Figure 6a displays the first three CV curves of the $NiMoO_4$ NS electrode. In the first CV curve, an intense cathodic peak located at approximately 0.25 V could be assigned to the lithium insertion reaction, which could be the reduction of $Ni^{2+}$ and $Mo^{6+}$ to form Ni, Mo, and $Li_2O$, as in Equation 5. The following two oxidation peaks were in the first CV curve located at 1.48 and 2.25 V, which can be attributed to the extraction process of $Li^+$ to form NiO and $MoO_3$, respectively (Equations 6 and 7).

$$8Li \rightarrow 8Li^+ + 8e^- \quad (4)$$

$$NiMoO_4 + 8Li^+ + 8e^- \rightarrow Ni + Mo + 4Li_2O \quad (5)$$

$$Ni + Li_2O \rightarrow NiO + 2Li^+ + 2e^- \quad (6)$$

$$Mo + 3Li_2O \rightarrow MoO_3 + 6Li^+ + 6e^- \quad (7)$$

In the subsequent lithiation processes, the decrease in the peak intensity and the position change indicate the irreversible Li-ion loss due to the SEI formation during the first cycle. Two pairs of redox peaks at 1.48/1.0 V and 2.25/1.75 V correspond to the reduction/oxidation of $MoO_3$ and NiO, respectively. Meanwhile, there is no obvious structural modification of the CV shapes, indicating the good electrochemical reversibility after the first cycling. Figure 6b shows the representative charge-discharge curves of the $NiMoO_4$ NS electrodes at a current density of 0.2 A $g^{-1}$, which is in agreement with the results of the CV curves. The first discharge and charge capacities can be achieved at 1,688 mA h $g^{-1}$ and 1,059 mA h $g^{-1}$ (Coulombic Efficiency, 62.7%), respectively. The low initial coulombic efficiency can be attributed to a common disadvantage regarding the formation of the SEI layer for metal oxide- based anode materials.

To evaluate the rate capability, the $NiMoO_4$ NS electrode was cycle tested at various current densities ranging from 0.2 to 8 A $g^{-1}$ (Figure 6c). Note that irreversible capacity losses occurred during the first several cycles, which is presumably attributed to decomposition of the electrolyte and/or solvent.[45] As expected, the reversible capacity of $NiMoO_4$ NSs was as high as 870 mA h $g^{-1}$ after ten cycles at 0.2 A $g^{-1}$. Upon increasing the current densities to 8 A $g^{-1}$ (the corresponding times of the charge-discharge processes are only 169 s), the average reversible capacities of $NiMoO_4$ NSs can be perfectly maintained at 370 mA h $g^{-1}$. This value is higher than most of the nickel oxide[16,46,47] and

molybdenum oxide anodes reported.[48,49] Furthermore, the capacity reverted to 900 mA h $g^{-1}$ when the current densities returned to 0.2 A $g^{-1}$, demonstrating the excellent rate performance.

To eliminate the capacity contribution from the Ni foam substrate, the rate capability of the bare Ni foam electrode was tested under the same current densities (Figure S7, Supporting Information). The first charge capacity of the nickel foam electrode was 161 mA h $g^{-1}$ at 0.2 A $g^{-1}$, and the capacity rapidly decreased to 25 mA h $g^{-1}$ when the current densities increased to 8 A $g^{-1}$ in the subsequent cycles, indicating that the capacities derived from the nickel foam substrate are negligible compared with the total capacity of $NiMoO_4$ NSs. Similar findings have also been demonstrated in our previous study.[17] Figure 6d presents the cycling performance and coulomb efficiency of the $NiMoO_4$ NS electrode at a current density of 1 A $g^{-1}$. The coulombic efficiency rapidly increased to nearly 95% after the first cycle. After 200 cycles, the discharge capacities of the $NiMoO_4$ NS electrode were stable at approximately 680 mA h $g^{-1}$, and no capacity decay was observed. Therefore, the as-prepared $NiMoO_4$ NS electrode also demonstrated superior electrochemical properties for high-performance and high-power LIBs.

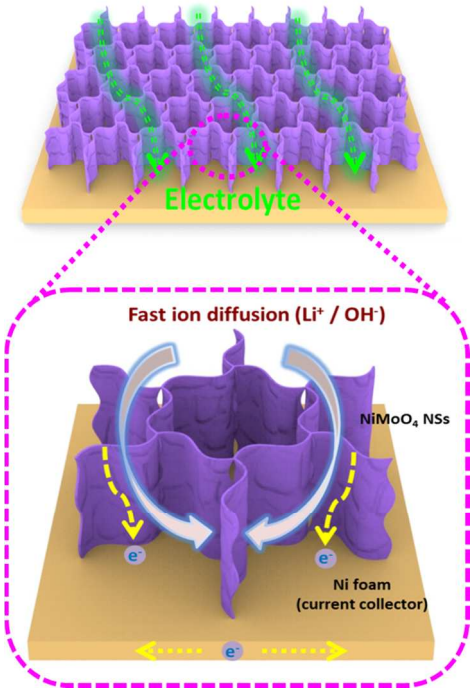


**Figure 7.** Schematic of the application advantages of the $NiMoO_4$ NSs on Ni foam.

These results prove the high capacitance, excellent rate capability and long-term cycling capability of the honeycomb-like $NiMoO_4$ NSs for high-performance SCs and LIBs. The superior electrochemical performance can be attributed to the honeycomb-like $NiMoO_4$ NSs with a unique morphology and structure that provide many benefits, as shown in Figure 7, including: (i) The $NiMoO_4$ NSs with abundant open spaces provide high surface area, increasing the contact area between the electrolyte and electrode. (ii) The ultrathin NSs significantly shorten the ion ($OH^-$ or $Li^+$) diffusion length, improving the rate performance. (iii) The $NiMoO_4$ NSs directly grown on Ni foam offer effective electron transport pathways between the Ni foam substrates and every $NiMoO_4$ NSs and avoid the use of any binders or additives. (iv) The unique electrode architecture with robust adhesion can mitigate the mechanical degradation and volume expansion.

## 4. Conclusions

In summary, amorphous honeycomb-like $NiMoO_4$ ultrathin NSs were synthesized *via* a facile and scalable electrochemical process followed by thermal treatment. The ultrathin mesoporous $NiMoO_4$ NSs on Ni foam with strong adhesion were directly evaluated as a binder-free electrode for SCs and LIBs. The large open spaces between the interconnected mesoporous NSs provide more electroactive surface sites and a facile electron transmission path, resulting in the high specific capacity (1,694 F $g^{-1}$ at 1 A $g^{-1}$ and 1,220 F $g^{-1}$ at 50 A $g^{-1}$ in SCs, 870 mA h $g^{-1}$ at 0.2 A $g^{-1}$ and 370 mA h $g^{-1}$ at 8 A $g^{-1}$ in LIBs) with outstanding rate performance and excellent cycling stability (92.7% after 9,000 cycles in SCs, and no capacity decay after 200 cycles in LIBs). In contrast to the previously reported hydrothermal processes, the electrochemical process is rapid and easily performed. Our study presents not only a promising difunctional electrode material for high-performance energy storage but also a simple and general fabrication process to design other binary metal oxide nanostructured electrodes for energy storage devices.

## Acknowledgements

This study was supported by the National Science Fund for Distinguished Young Scholars of China (no. 21225625), the Pearl River Scholar Program of the Guangdong Province and the Australian Research Council (ARC) through the Future Fellow Program (FT140100757).

## Notes and references

[a]*School of Chemistry & Chemical Engineering, South China University of Technology, No. 381 Wushan Road, Guangzhou 510640,People's Republic of China; E-mail: lxding@scut.edu.cn, hhwang@scut.edu.cn;*
[b]*School of Chemical Engineering, The University of Adelaide, Adelaide, SA 5005, Australia.*

†Electronic Supplementary Information (ESI) available: [XRD pattern, XPS, EDX, CV curves of Ni foam and $NiMoO_4$ NSs, SEM image of the $NiMoO_4$ Nss electrode after 9000 cycles, and the capacity of nickel foam electrode]. See DOI: 10.1039/b000000x/

1 B. Dunn, H. Kamath, J. Tarascon, *Science*, 2011, **18**, 928.
2 Z. Yang, J. Zhang, M. Kintner-Meyer, X. Lu, D. Choi, J. Lemmon, J. Liu, *Chem. Rev.*, 2011, **111**, 3577.
3 P. Simon, Y. Gogotsi, *Nat. Mater.*, 2008, **7**, 845.
4 J. M. Tarascon, M. Armand, *Nature*, 2001, **414**, 359.
5 H. Wang, H. S. Casalongue, Y. Liang, H. Dai, *J. Am. Chem. Soc.*, 2010, **132**, 7472.
6 D. Pech, M. Brunet, H. Durou, P. Huang, V. Mochalin, Y. Gogotsi, P. L. Taberna and P. Simon, *Nat. Nanotechnol.*, 2010, **5**, 651.
7 R. R. Salunkhe, J. J. Lin, V. Malgras, S. X. Dou, J. H. Kim, Y. Yamauchi, *Nano Energy*, 2015, **11**, 211.
8 L. Zhu, H. J. Peng, J. Y. Liang, J. Q. Huang, C. M. Chen, X. F. Guo, W. C. Zhu, P. Li, Q. Zhang, *Nano Energy*, 2015, **11**, 746.
9 L. Li. Z. Wu, S. Yuan. X. B. Zhang, *Energy Environ. Sci.*, 2014, **7**, 2101.
10 10 Z. l. Wang, D. Xu, Y. Huang, Z. Wu, L. M. Wang, X. B. Zhang, *Chem. Commun.*, 2012, **48**, 976.

11 J. X. Qiu, C. Lai, S. Li, S. Q. Zhang, *RSC Adv.*, 2014, **4**, 18899.
12 S. Li, J. X. Qiu, C. Lai, M. Ling, H. J. Zhao, S. Q. Zhang, *Nano Energy*, 2015, **12**, 2244
13 V. Chabot, D. Higgins, A. P. Yu, X. C. Xiao, Z. W. Chen, J. J. Zhang, *Energy Environ. Sci.*, 2014, **7**, 1564.
14 G. Wang, L. Zhang, J. J. Zhang, *Chem. Soc. Rev.*, 2012, **41**, 797.
15 M. H. Yu, W. Wang, C. Li, T. Zhai, X. H. Lu Y. X. Tong, *NPG Asia Mater.*, 2014, **6**, 129.
16 S. H. Choi, Y. N. Ko, J. K. Lee, Y. C. Kang, *Sci. Rep.*, 2014, DOI:10.1038/srep05786
17 D. D. Li, L. X. Ding, S. Q. Wang, D. D. Cai H. H. Wang, *J. Mater. Chem. A*, 2014, **2**, 5625.
18 L. Zhan, S. Q. Wang, L. X. Ding, Z. Li, H. H. Wang, *Electrochim. Acta*, 2014, **135**, 35.
19 Z. Y. Wang, L. Zhou, X. W. Lou, *Adv. Mater.*, 2012, **14**, 1903.
20 M. H. Chen, J. L. Liu, D. L. Chao, J. Wang, J. H. Yin, J. Y. Lin, H. J. Fan, Z. X. Shen, *Nano Energy*, 2014, **9**, 364.
21 X. H. Lu, Y. X. Zeng, M. H. Yu, T. Zhai, C. L. Liang, S. L. Xie, M. S. Balogun, Y. X. Tong, *Adv. Mater.*, 2014, **26**, 3148.
22 H. G. Wang, D. L. Ma, Y. Huang, X. B. Zhang, *Chem. Eur. J.*, 2012, **18**, 8987.
23 Z. L. Wang, D. Xu, J. J. Xu, X. B. Zhang, *Chem. Soc. Rev.*, 2014, **43**, 7746.
24 L. Q. Mai, F. Yang, Y. L. Zhao, X. Xu, L. Xu, Y. Z. Luo, *Nat. Commun.*, 2011, **2**, 381.
25 X. Z. Yu, B. G. Lu, Z. Xu, *Adv. Mater.*, 2014, **26**, 1044.
26 D. P. Cai, B. Liu, D. D. Wang, L. L. Wang, Y. Liu, H. Li, Y. R. Wang, Q. H. Li, T. H. Wang, *J. Mater. Chem. A*, 2014, **2**, 4954.
27 J. Haetge, I. Djerdj, T. Brezesinski, *Chem. Commun.*, 2012, **48**, 6726.
28 W. Xiao, J. S. Chen, C. M. Li, R. Xu, X. W. Lou, *Chem. Mater.*, 2010, **22**, 746.
29 D. Ghosh, S. Giri, C. K. Das, *Nanoscale*, 2013, **5**, 10428.
30 M. C. Liu, L. B. Kong, C. Lu, X. J. Ma, X. M. Li, Y. C. Luo, L. Kang, *J. Mater. Chem. A*, 2013, **1**, 1380.
31 D. P. Cai, D. D. Wang, B. Liu, Y. R. Wang, Y. Liu, L. L. Wang, H. Li, H. Huang, Q. H. Li, T. H. Wang, *ACS Appl. Mater. Inter.*, 2013, **5**, 12905.
32 S. J. Peng, L. L. Li, H. B. Wu, S. Madhavi, X. W. Lou, *Adv. Energy Mater.*, 2014, DOI: 10.1002/aenm.201401172
33 K. Xiao, J. W. Li, G. F. Chen, Z. Q. Liu, N. Li, Y. Z. Su, *Electrochim. Acta*, 2014, **149**, 341348.
34 J. Yan, Z. J. Fan, W. Sun, G. Q. Ning, T. Wei, Q. Zhang, R. F. Zhang, L. J. Zhi, F. Wei, *Adv. Funct. Mater.*, 2012, **22**, 2632.
35 Z. Wu, X. L. Huang, Z. L. Wang, J. J. Xu, H. G. Wang, X. B. Zhang, *Sci. Rep.*, 2014, **4**, 3669
36 B. Cui, H. Lin, Y. Z. Liu, J. B. Li, P. Sun, X. C. Zhao, C. J. Liu, *J. Phys. Chem. C*, 2009, **113**, 14083.
37 G. G. Zhang, W. F. Li , K. Y. Xie, F. Yu, H. T. Huang, *Adv. Funct. Mater.*, 2013, **23**, 3675.
38 C. Z. Yuan, J. Y. Li, L. R. Hou, X.G. Zhang, L. F. Shen, X. W. Lou, *Adv. Funct. Mater.*, 2012, **22**, 4592.
39 X. H. Lu, T. Y. Liu, T. Zhai, G. M. Wang, M. H. Yu, S. L. Xie, Y. C. Ling, C. L. Liang, Y. X. Tong, Y. Li, *Adv. Energy Mater.*, 2014, DOI: 10.1002/aenm.201300994.
40 Y. Qian, R. Liu, Q. F. Wang, J. Xu, D. Chen, G. Z. Shen, *J. Mater. Chem. A*, 2014, **2**, 10917.
41 W. Hong, J. Q. Wang, P. W. Gong, J. F. Sun, L. Y. Niu, Z. G. Yang, Z. F. Wang, S. R. Yang, *J. Power Sources*, 2014, **270**, 516.
42 H. B. Li, M. H. Yu, F. X. Wang, P. Liu, Y. Liang, J. Xiao, C. X. Wang, Y. X. Tong, G. W. Yang, *Nat. Commun.*, 2013, **4**, 1894.
43 Y. Z. Su, K. Xiao, N. Li, Z. Q. Liu, S, Z. Qiao, *J. Mater. Chem. A*, 2014, **2**, 13845.
44 F. Luan, G. M. Wang, Y. C. Ling, X. H. Lu, H. Y. Wang, Y. X. Tong, X. X. Liu, Y. Li, *Nanoscale*, 2013, **5**, 7984.
45 Y. S. Luo, J. S. Luo, J. Jiang, W. W. Zhou, H. P. Yang, X. Y. Qi, H. Zhang, H. J. Fan, Denis Y. W. Yu, C. M. Li, T. Yu, *Energy Environ. Sci.*, 2012, **5**, 6559.
46 X. L. Sun, W. P. Si, X. H. Liu, J. W. Deng, L. X. Xi, L. F. Liu, C. L. Yan, O. G. Schmidt, *Nano Energy*, 2014, **9**, 168.
47 Z. C. bai, Z. C. Ju, C. L. Guo, Y. T. Qian, B. Tang, S. L. Xiong, *Nanoscale*, 2014, **6**, 3268.
48 T. Tao, A. M. Glushenkov, C. F. Zhang, H. Z. Zhang, D. Zhou, Z. P. Guo, H. K. Liu, Q. Y. Chen, H. P. Hu, Y. Chen, *J. Mater. Chem.*, 2011, **21**, 9350.
49 Y. N. Ko, S. B. Park, K. Y. Jung, Y. C. Kang, *Nano Lett.*, 2013, **13**, 5462.

**Graphical abstract**